Progress In Electromagnetics Research B, Vol. 39, 39–53, 2012

INVERSE SCATTERING SHAPE RECONSTRUCTION OF 3D BACTERIA USING THE LEVEL SET ALGORITHM

A. M. Hassan[1,*], M. R. Hajihashemi[2], and M. El-Shenawee[1]

[1]Department of Electrical Engineering, University of Arkansas, Fayetteville, AR 72703, USA

[2]Department of Biomedical Engineering, University of Florida, Gainesville, FL 32611, USA

Abstract—Bacteria exist in a variety of groups of shapes, sizes, and single or multiple cell formations. In this paper, the level set shape reconstruction technique, the method of moments, and the marching cubes methods are integrated in the high frequency band for imaging three dimensional bacteria. The time step and the resolution of the marching cubes method are investigated to smooth the error function of the level set and hence speed up the convergence at high frequencies. The numerical results demonstrate the robustness of the level set algorithm for the detection of bacteria based on their shapes. The three dimensional shape reconstructions of unknown bacteria can be utilized to classify biological warfare agents.

1. INTRODUCTION

Biological warfare agents (BWA) pose serious threats on humankind as exemplified by the lethal international incidents in Japan, Russia and the USA [1]. The threat could be magnified by the fact that there are currently limited accurate tests that can identify biological warfare agents in a time frame small enough to launch effective counter measures [1].

Several modalities were investigated to lower the detection and classification process time of biological warfare agents such as acoustical, electrochemical, piezoelectric, thermal and optical techniques [2–4]. The optical technique is classified as indirect or

Received 21 December 2011, Accepted 12 February 2012, Scheduled 20 February 2012

* Corresponding author: Ahmed M. Hassan (amhassan@uark.edu).

direct, depending on whether a labeling agent is used or not [2]. Examples of direct optical methods are resonant mirror (RM) and evanescent wave interferometer (EWI) whereas the indirect optical methods include the fluorescent labeled antibody (FA). The RM is based on placing a high refractive index layer on top of a glass prism with a low refractive index material inserted in the middle as a coupler [3]. Once the light is exerted at a certain angle it exhibits total internal reflection in the high refractive index layer. In addition, evanescent waves will propagate perpendicular to the high refractive index layer into the sensing medium above it. Biological agents positioned on top of the high refractive index layer interact with the evanescent wave perturbing the reflected waves from the prism and allowing the detection of the agent [3]. The performance of the RM technique was tested using the Staphylococcus Aureus bacteria exhibiting a limited detection of 10^6 cells/ml. Similarly, EWI uses evanescent waves, in addition to utilizing optical elements, to create interference patterns from the sensing region [4]. In indirect methods, labeling agents are utilized to target certain elements, termed immunoglobulins, in BWA [2]. The labeling agents are excited by the light at a short wave length and then release light at a longer wavelength to enhance the signature of the agent [2].

The above techniques were based on spectroscopy, where the presence of BWA were identified using the absorption resonances in the transmission spectra of the sample. Advances in micro-fabrication and micro-fluidics had facilitated the development of systems to allow 3D tomography of a single cell [5, 6]. In the cell tomography system developed by Meyera et al., cell samples were rotated from 0° to 360° in steps of 0.72° in order to achieve 500 projections [5]. A three dimensional filtered back-projection algorithm was implemented to reconstruct the shape of cancerous cells [6].

The current work expands the previous published work on the level set method [7–10]. The contribution can be summarized as: (i) demonstrating the capability of the level set algorithm for the shape reconstruction of 3D bacteria, leading to use very high frequencies, (ii) testing the convergence of the algorithm at frequencies up to 300 THz, and (iii) investigating and analyzing the effect of two specific parameters on the algorithm convergence at these high frequencies; these parameters are the time step and the resolution of the marching cubes method.

The proposed idea is based on reconstructing the 3D shape of bacteria as a tool of detection, since biological agents have very different shapes. Bacteria, for example, can exist in three fundamental shapes; (i) spherical (coccus), (ii) rod (bacillus), and (iii) spiral

(spirillum) [11], in single, pairs (diplo-), groups of cells, or in chains (Strepto-). In general, bacteria can be separated, joined, or overlapped depending on their species [11].

Finally, different bacteria have different sizes ranging from 100 nm to 80 µm [11]. This small size of bacteria requires the use of high frequencies at the upper limit of the terahertz (THz) and in the infrared (IR) band. The shape reconstruction of 3D bacteria can help narrowing down the possible categories of the bacteria under test in a fast manner. The conventional techniques can be lengthy and require larger samples of the bacteria. The exact classification can then be determined using conventional techniques such as polymerase chain reaction (PCR) which detects and amplifies the genetic material needed to identify the bacteria [2].

In this work, we employ the high frequency 3D level set algorithm to reconstruct the shape of BWA immersed in air. As reported in [12], the BWA are most effectively delivered as aerosols in air and they represent a serious threat because they are invisible and tasteless. However, investigating bacteria immersed in other media is also important for validation with controlled laboratory measurements similar to those conducted in [5, 6]. The later will be the subject of future work. The current work represents the first attempt to prove the concept of detecting harmful bacteria based on their shapes using the high frequency 3D level set algorithm. Fig. 1 shows a synthetic system to collect the scattering fields at different incident and receiving directions (angles) and at multiple high frequencies, conceptually similar to the single cell system in [5, 6]. The single cell system reported in [5] demonstrated that the 3D shape reconstruction increased the accuracy of cancer cells detection three fold, compared with the 2D shape reconstruction. Therefore, the current 3D shape reconstruction of bacteria has a high potential for the detection and

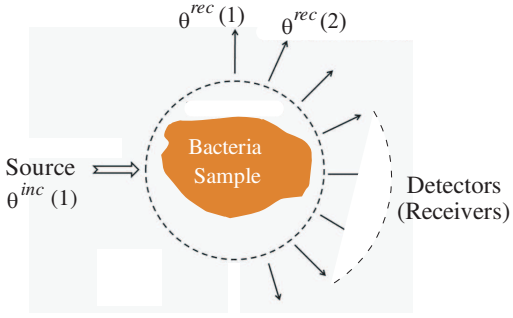

Figure 1. A synthetic setup showing the high frequency source and the detectors directions.

classification of these bacteria.

2. LEVEL SET SHAPE RECONSTRUCTION ALGORITHM

The level set inverse scattering technique has proven its capability in retrieving the shapes of multiple unknown targets based on their scattered fields in the microwave range of frequency (100 MHz–10 GHz) [7–10]. The scattered fields are measured at multiple receiving directions when the target is excited from multiple incident directions and at multiple frequencies (see Fig. 1). The algorithm starts with an initial guess which then evolves to the true target. The main idea behind the level set technique is that the evolving object is implicitly modeled as the zero level of a higher order function [7–10]. The zero level of a higher order function ϕ is given as:

$$\Gamma_t = \{\bar{r} | \, \phi(\bar{r}, t) = 0\} \tag{1}$$

where Γ_t represents the surface of the evolving object and $\bar{r}(x, y, z)$ represents the location vector in the computational domain. The level set function, ϕ, is updated according to the Hamilton Jacobi equation:

$$\frac{\partial \phi}{\partial t} + F(\bar{r}) \|\nabla \phi\| = 0, \qquad \phi_0 = \phi(\bar{r}, t = 0) \tag{2}$$

where $F(\bar{r})$ is the normal *deformation velocity* and ϕ_0 represents the initial values of the level set function. The initial values of the level set function, ϕ_0, at each pixel in the computational domain are assigned equal to the signed distance function which is defined as the minimum distance between each pixel and the surface (or contour) of the initial guess [7–10]. The signed distance function is negative if the pixel is inside the initial guess surface, positive if the pixel is outside the initial guess surface and zero if the pixel is on the surface of the initial guess. The deformation velocity function $F(\bar{r})$ normal to the surface is the force which drives the initial surface to converge to the true one. The values of the normal *deformation velocity* are calculated by minimizing the mismatch between the simulated fields scattered from the evolving object and the synthetic measured fields, see details in [7–10]. In order to calculate $F(\bar{r})$, the method of moments surface current densities and the *marching cubes* computer graphics method are used. Details of the 3D level set algorithm are given in [10]. It should be mentioned that the level set algorithm requires solving the scattering problem twice; once for the forward problem and the second for the adjoint problem [13]. The forward scattered fields are the fields scattered from the evolving object due to a normalized incident plane wave. The adjoint fields are the fields scattered from the evolving object due to an incident plane

wave of amplitude equal to the complex conjugate of the difference between the simulated scattered fields from the evolving object and the synthetic measurements from the true object [13]. The forward and adjoint scattered far fields are used to update the deformation velocity $F(\bar{r})$ according to the following equation:

$$F(\bar{r}) = -\sum_{i=1}^{N_{\text{inc}}}\sum_{j=1}^{N_{\text{rec}}} \text{Re}\left(\bar{M}(\bar{r})\cdot\bar{M}'(\bar{r}) - \frac{\nabla\cdot\bar{J}(\bar{r})\ \ \nabla\cdot\bar{J}'(\bar{r})}{(\omega\varepsilon_0)^2}\right) \tag{3}$$

where N_{inc} is the number of incident directions, N_{rec} is the number of receiving directions, $\bar{M}(\bar{r}), \bar{M}'(\bar{r}), \bar{J}(\bar{r})$ and $\bar{J}'(\bar{r})$ are the forward magnetic current density, adjoint magnetic current density, forward electric current density, and adjoint electric current density, respectively. The deformation velocity F is calculated at the surface of the evolving object. However, from (2), F needs to be calculated at every pixel in the computational domain in order to update the level set function. Therefore, the extended deformation velocity is calculated such that its value at each pixel in the domain is equal to the deformation velocity at the closest pixel on the surface (or the contour) [7–10]. The Hamilton Jacobi equation in (2) is discretized spatially and temporally as follows:

$$\phi_{ijk}^{n+1} = \phi_{ijk}^{n} - \Delta t\left[\max(F_{ijk},0)\nabla^{+} + \min(F_{ijk},0)\nabla^{-}\right] \tag{4a}$$

where i, j, k are the discretization indices for the x, y, z directions, respectively, Δt is the time step, F_{ijk} is deformation velocity obtained using (3), ∇^{+}, and ∇^{-} are spatial difference operators, e.g., ∇^{+} is given by [10]:

$$\nabla^{+} = \left[\max\left(D_{ijk}^{x-},-D_{ijk}^{x+},0\right)^2 + \max\left(D_{ijk}^{y-},-D_{ijk}^{y+},0\right)^2 + \max\left(D_{ijk}^{z-},-D_{ijk}^{z+},0\right)^2\right]^{1/2} \tag{4b}$$

where $D_{ijk}^{x\pm}$, $D_{ijk}^{y\pm}$, and $D_{ijk}^{z\pm}$ are the forward and backward difference spatial operators [10]. The operator ∇^{-} is similar to (4b) upon replacing the function max(.) with the function min(.) [10]. The temporal and spatial discretizations are constraint through the Courant condition to ensure the stability of the solution of (2) [7–10]. The cost function (i.e., the mismatch between the measured and the simulated fields) is given as:

$$Cost = \sum_{\theta^{\text{inc}},\varphi^{\text{inc}}}\sum_{\theta^{\text{rec}},\varphi^{\text{rec}}} \frac{\left\|\bar{E}_{\text{evolv}}\left(\theta^{\text{inc}},\varphi^{\text{inc}},\theta^{\text{rec}},\varphi^{\text{rec}}\right) - \bar{E}_{\text{true}}\left(\theta^{\text{inc}},\varphi^{\text{inc}},\theta^{\text{rec}},\varphi^{\text{rec}}\right)\right\|^2}{\left\|\bar{E}_{\text{true}}\left(\theta^{\text{inc}},\varphi^{\text{inc}},\theta^{\text{rec}},\varphi^{\text{rec}}\right)\right\|^2} \tag{5}$$

where $\bar{E}_{\text{evolv}}$ and $\bar{E}_{\text{true}}$ are the simulated electric far fields scattered from the evolving object and the measured far fields from the true object, respectively. The angles θ^{inc}, ϕ^{inc} and θ^{rec}, ϕ^{rec} represent the incident and scattering directions, respectively, (see Fig. 1).

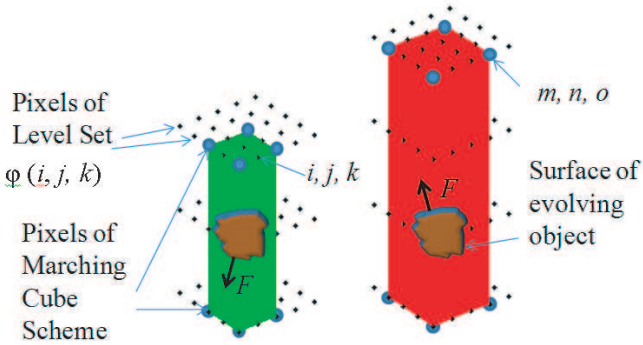

Figure 2. 3D configuration of the level set method, marching cubes scheme, and evolving surface, showing (a) $3 \times 3 \times 3$ (see the pixels on the green cube), and (b) $4 \times 4 \times 4$ (see the pixels on the red cube), level set pixels down sampled to one marching cube with $2 \times 2 \times 2$ pixels.

The MoM surface nodes on the evolving object need to be updated in every inversion iteration. Therefore, the marching cubes scheme is implemented for the 3D targets [10]. The configuration of Fig. 2 shows the pixels (i, j, k) in the computational domain that are used for updating the level set function $\varphi(i,\ j,\ k)$, while the pixels $(m,\ n,\ o)$ are associated with the marching cubes scheme for updating the MoM surface nodes. To keep the computational cost intact, finer resolution is typically used for the level set pixels (i, j, k) compared with those used for the marching cubes pixels $(m,\ n,\ o)$. For example, in Figs. 2(a) and 2(b), each $3 \times 3 \times 3$ and $4 \times 4 \times 4$ level set pixels, respectively, are down sampled to one marching cube with $2 \times 2 \times 2$ pixels [10].

3. NUMERICAL RESULTS

In all results here, 26 incident and 26 receiving directions are utilized (similar to our work in [10]), where the θ^{inc} and θ^{rec} angles vary from 0 to π in steps of $\pi/4$ and vary the ϕ^{inc} and ϕ^{rec} angles vary from 0 to 2π in steps of $\pi/4$. Moreover, the dielectric properties of bacteria are assumed here to be similar to the water. This assumption is motivated by the availability of water properties in the terahertz and the infrared bands (see [14] for the range 15 THz–150 THz, [15] for the range 5 GHz–30 THz, and [16] for the range 114–833 THz). Also, this approximation has been utilized in the literature at lower frequencies and can be justified by the fact that water constitutes the majority of the cellular contents [17]. The dielectric properties of water versus

frequency are shown in Fig. 3. It is well known that water is dispersive in the terahertz and infrared bands [14–16]. However, it is important to emphasize that the 3D level set shape reconstruction algorithm is not limited to certain material properties as long as they are *a priori* known at each frequency used in the reconstruction algorithm.

As published in the literature (e.g., [7–10, 18]), the level set method has been proven to be robust. Therefore the algorithm always converges to the true target regardless of the initial guess. During the reconstruction, a single initial guess could evolve and break into several objects or the multiple objects initial guess could merge into

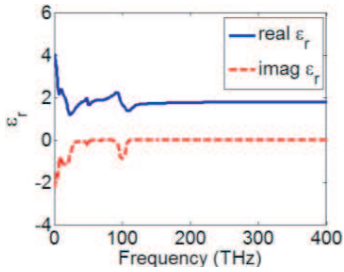

Figure 3. The dielectric relative permittivity of water [14–16].

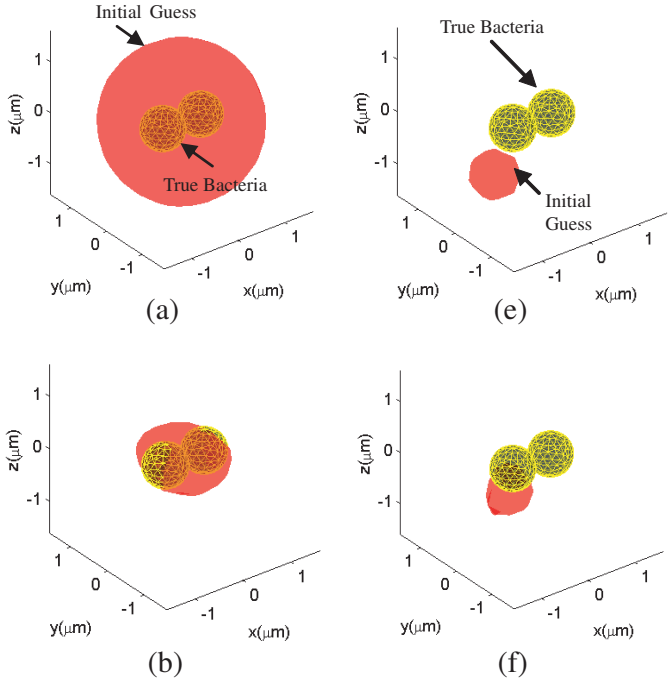

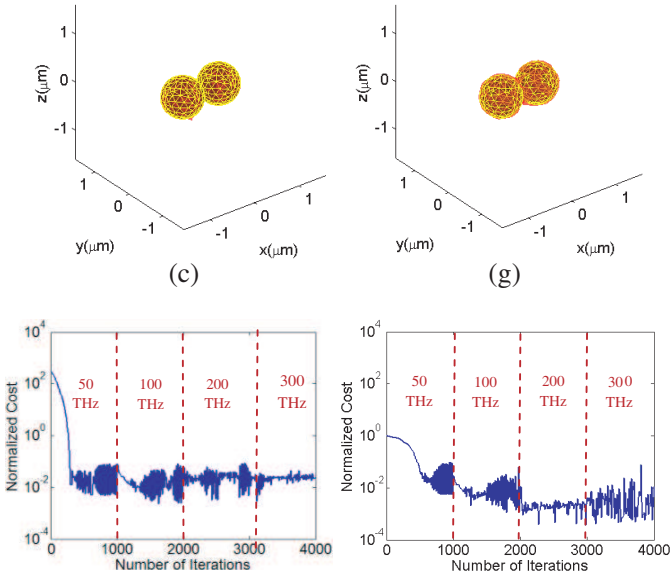

Figure 4. Reconstruction results of diplococci bacteria using the first initial guess: (a) The first initial guess versus the true diplococci bacteria. (b) The level set reconstruction after 250 iterations at 50 THz. (c) The final level set reconstruction after 4000 iterations at 300 THz. (d) The normalized cost function versus the iteration number, using frequency hopping 50–300 THz. The results of (a)–(d) are repeated in (e)–(h) using a different initial guess. The evolving object is shown in red color and the true diplococci bacteria are shown in yellow mesh.

a single object. When the initial guess was different in shape and far in location from the true target, more iterations and frequencies were needed; however, the evolving object always converged to the true one [7–10]. The initial guess was also selected as four spheres, they merged into one sphere demonstrating the successful convergence of the level set algorithm in the work by Dubios et al. [18]. Therefore for simplicity in this work, the initial guess of the 3D bacteria was selected to be a sphere of radius 1.5 μm located at the center of the computational domain.

Figure 4 shows the 3D reconstruction of the diplococci bacteria of diameter of 0.8 μm and separation gap 10 nm. Four frequencies are used in the frequency hopping scheme in this case, as 50 THz, 100 THz, 200 THz and 300 THz. Hopping from one frequency to the next one

was conducted after 1000 iterations [10]. Even though the normalized cost function in Fig. 4(d) seems constant after 250 iterations, on the average, the evolving object is still significantly improving up to 4000 iterations. The reconstruction result after 250 iterations is shown in Fig. 4(b) while the final reconstruction after 4000 iterations is shown in Fig. 4(c). The results of Fig. 4(a)–(d) are repeated using another initial guess as a sphere of radius 0.5 µm located at (0 µm, 1 µm, −1.5 µm) as shown in Figs. 4(e)–(h). The initial guess in this case is smaller than the true target and located off the center of the computational domain by 1 µm in the y-direction and −1.5 µm in the z-direction.

While the large oscillations in the cost function, in Figs. 4(d) and 4(h), obscure the convergence of the algorithm, it is observed that increasing the number of iterations at each frequency and using more frequencies improve the reconstruction results. The reconstruction of the diplococcic bacteria in Fig. 4 required $\sim$ 10 hours using a single core on a node with 2 Xeon X5670 processors having a clock speed of 2.93 GHz and 24 GB of memory. The results in Fig. 4 show good agreement with the true shape of the diplococci bacteria, but no techniques are implemented to smooth out the cost function.

To focus the current work on understanding and mitigating the large oscillations observed in the cost function at the used high frequencies necessary for the bacteria detection, we adopted a simple hopping criteria based on pre-assigned number of iterations at each frequency selected based on the numerical experience with the application (1000 iterations in this work). It was observed that the cost function oscillations prevent reaching the pre-assigned stopping criterion of 10^{-7} [9]. In our previous work in the microwave band [7–10], the cost function oscillations were manageable. Therefore, we implemented better hopping criteria to avoid unnecessary increase in the computational time when the cost function drops in local minima. The criterion was based on the most recent 20 samples calculated for the cost function. If the difference between the averages of each successive points was less than a threshold (e.g., 1%), the working frequency hops to a higher value [10]. These criteria can be easily adopted for the bacteria detection in this work.

The results in Figs. 4(d) and 4(h) demonstrate large magnitude of oscillations in the normalized cost function, especially as the frequency increases, which affects the convergence of the algorithm. To mitigate these oscillations, two specific parameters are investigated; the time step, Δt, and the resolution of the marching cubes scheme as explained in Fig. 2. The results of Fig. 5 will demonstrate the decrease in the magnitude of the observed oscillations and hence the improvement in the algorithm convergence versus these two parameters.

A chain of three bacillus bacteria each having a length of 3 μm and a diameter of 1 μm with separation gap of 0.01 μm are shown in Fig. 5. Six hopping frequencies are used in this case, as 10, 25, 50, 60, 70, and 85 THz. Higher frequencies, up to 150 THz, were tested in the reconstruction of the three bacillus bacteria in Fig. 5 (not shown); however, insignificant improvement in the results was achieved at frequencies higher than 85 THz. The initial guess is a sphere of radius

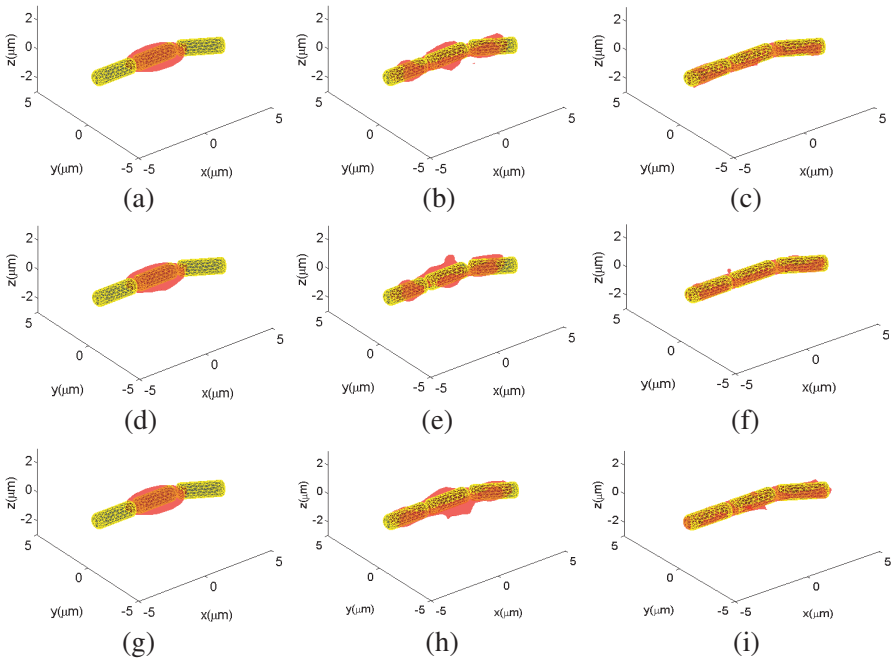

Figure 5. (a)–(c) Reconstruction of a chain of three bacillus bacteria using $7 \times 7 \times 7$ pixels at all frequencies down sampled to a one marching cube with time step (Δt). (a) After 1000 iterations at 10 THz. (b) After 3000 iterations at 50 THz. (c) Final reconstruction after 6000 at 85 THz. (d)–(f) Reconstruction using $7 \times 7 \times 7$ pixels at all frequencies down sampled to a one marching cube and half the time step ($\Delta t/2$). (d) After 1000 iterations at 10 THz. (e) After 3000 iterations at 50 THz. (f) Final reconstruction after 6000 iterations at 85 THz. (g)–(i) Reconstruction using progressively decreasing number of pixels from $7 \times 7 \times 7$ to $5 \times 5 \times 5$ down sampled to a one marching cube and the time step (Δt). (g) After 1000 iterations at 10 THz. (h) Reconstruction after 3000 iterations at 50 THz. (i) Final reconstruction after 6000 at 85 THz. The evolving object is shown in red color and the true bacillus bacteria are shown in yellow mesh.

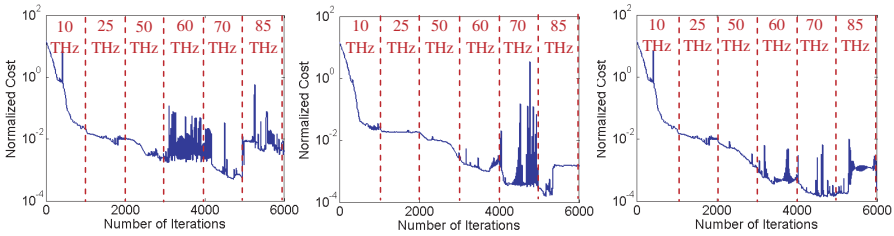

Figure 6. The reconstruction cost functions of a chain of three bacillus bacteria. (a) Using $7 \times 7 \times 7$ pixels at all frequencies down sampled to a one marching cube and time step (Δt). (b) Using $7 \times 7 \times 7$ pixels at all frequencies down sampled to a one marching cube and half the time step used in $6a$ ($\Delta t/2$). (c) Using progressively decreasing number of pixels from $7 \times 7 \times 7$ to $5 \times 5 \times 5$ down sampled to a one marching cube and time step (Δt).

2 µm located at the center of the computational domain. Figs. 5(a)–(i) show the reconstruction results of the three bacillus bacteria after 1000, 3000, and 6000 iterations. The cost functions are shown in Fig. 6. Similar to Figs. 4(d) and 4(h), it is observed that the normalized cost function (mismatch) is highly oscillating around 60 THz as shown in Fig. 6(a). The reconstruction of the three bacillus chain of Figs. 5(a)–(c) is repeated in Fig. 5(d)–(f) using $\Delta t/2$. The corresponding cost function is shown in Fig. 6(b). The results in Fig. 6(b) show a decrease in the oscillations level of the cost function as the time step decreases, especially around the 60 THz. It is important to note that although the reduction in the time step has mitigated the oscillations at 60 THz shown in Fig. 6(a), these oscillations are still observed around 70 THz in Fig. 6(b). Therefore, the second parameter, the resolution of the marching cubes was investigated as demonstrated in Fig. 6(c) associated with Figs. 5(g)–(i) which used the larger time step Δt.

As discussed earlier, this factor determines the resolution of the MoM surface nodes of the evolving object. In Figs. 5(a)–(f) every $7 \times 7 \times 7$ level set pixels are down sampled to one marching cube at all eight frequencies. However, in Figs. 5(g)–(i), an empirical frequency based down sampling scheme is used as follows; at 10 THz and 25 THz, every $7 \times 7 \times 7$ level set pixels are down sampled to a one marching cube; at 50 THz and 60 THz, every $6 \times 6 \times 6$ level set pixels are down sampled to a one marching cube; and at 70 THz and 85 THz, every $5 \times 5 \times 5$ level set pixels are down sampled to a one marching cube. The corresponding cost function is shown in Fig. 6(c) which shows the decrease of the oscillations level upon increasing the marching cubes

resolution at all considered frequencies. The reconstruction CPU times for the results in Figs. 5(a)–(c), Figs. 5(d)–(f), and Figs. 5(g)–(i) are $\sim$ 19 hrs, 25 hrs, and 56 hrs, respectively, also using a single core on a node with 2 Xeon X5670 processors having a clock speed of 2.93 GHz and 24 GB of memory. These reconstruction times can be significantly reduced via the MPI parallelization of the algorithm [19].

In this work, an implicit regularization scheme is implemented [10]. This regularization is based on weighted averaging of the deformation velocity and smoothing of the evolving surface meshes as reported in [10]. Specifically, the deformation velocity at each surface patch is calculated as the weighted average of the velocities of neighboring patches. The average deformation velocity at a particular patch is calculated by assigning a weight of three to the velocity at that patch and a weight of two to the velocities of the neighboring patches [10].

As known, due to the nonlinearity of the inverse scattering problem, the level set algorithm requires measurements at multiple sources and receivers as shown in Fig. 1. In our previous work, the level set algorithm has proven its capability in bistatic, monostatic, and limited view configurations in the microwave frequency range [7–10]. However, advances in micro-fabrication and micro-fluidics have allowed the development of systems that provide recordings every 0.72° in order to achieve several hundred measurements in the bistatic configuration at 510 THz [5]. Although the level set algorithm capability was proved using experimental data in the microwave frequency range [20, 21], the experimental validation of the results obtained in this work will require a coherent radiation system that can measure the amplitude and the phase at high frequencies. The work in [22] and [23] have demonstrated the development of a continuous coherent radiation system operating from the microwave region up to 40 THz. Moreover, for diffuse optical tomography applications, a coherent radiation system has been developed to operate at several discrete frequencies in the infrared frequency range from 300 THz to 450 THz [24]. Therefore, we believe that experimental validation of the high frequency level set algorithm for bacteria detection can be conducted in the near future using coherent systems similar to the ones reported in [22–24].

4. CONCLUSION

The obtained results demonstrated the capability of the high frequency level set algorithm in reconstructing the shapes of 3D bacteria for the purpose of detection. The robustness of the algorithm increased when the time step was decreased and when the resolution of the marching cubes was increased. The bacteria in this work were assumed to be

immersed in air; however, in future work the surrounding medium will be incorporated in the algorithm.

In this work, only synthetic data free of noise were examined using the level set algorithm at high frequencies. Experimental data of scattered fields from 3D bacteria are not available at this point; however, it is expected to be prone to several sources of noise such as white noise, drift noise due to the system configuration and the sensor stepping movements, if any, and clutter due to nearby unwanted objects, especially at high frequencies. For example, in our experimental microwave work [20], the drift noise due to the stepping rotation of the antennas was experienced. Low pass filtering techniques were successfully implemented to remove the drift noise [20]. Also, in the microwave band, the level set algorithm was successfully tested versus random noise added to the synthetic data with signal to noise ratio (SNR) as low as 5 dB [7, 10]. For lower values of SNR, obtaining meaningful reconstruction results of any target using almost any method will be challenging. In the future, the level set algorithm will be examined using experimental data in the high frequency, once made available from systems similar to those reported in [5, 6].

In the case that different types of bacteria exist, but not overlapping, the current level set algorithm is capable of reconstructing their shapes [10]. However, if the different types of bacteria are overlapping, which means that different materials targets are overlapping, the multiphase level set algorithm will be needed, which is a future work.

ACKNOWLEDGMENT

This work was sponsored by the Army Research Laboratory and was accomplished under Cooperative Agreement Number **W911NF-10-2-0093**. The views and conclusions contained in this document are those of the authors and should not be interpreted as representing the official policies, either expressed or implied, of the Army Research Laboratory or the U.S. Government. The U.S. Government is authorized to reproduce and distribute reprints for Government purposes notwithstanding any copyright notation herein.

REFERENCES

1. Scholl, P. F., M. A. Leonardo, A. M. Rule, M. A. Carlson, M. D. Antoine, and T. J. Buckley, "The development of matrix-assisted laser desorption/ionization time-of-flight mass spectrometry for the detection of biological warfare agent

aerosols," *Johns Hopkins APL Technical Digest*, Vol. 20, No. 3, 1999.

2. Ivnitski, D., I. Abdel-Hamid, P. Atanasov, and E. Wilkins, "Biosensors for detection of pathogenic bacteria," *Biosensors & Bioelectronics*, Vol. 14, 599–624, 1999.
3. Watts, H. J., C. R. Lowe, and D. V. Pollard-Knight, "Optical biosensor for monitoring microbial cells," *Anal. Chem.*, Vol. 66, 2465–70, 1994.
4. Schneider, B., J. Edwards, and N. Hartman, "Hartman interferometer: Versatile integrated optic sensor for label-free, real-time quantification of nucleic acids, proteins, and pathogens," *Clin. Chem.*, Vol. 43, No. 9, 1757–1763, 1997.
5. Meyera, M., M. Fauverb, J. Rahna, T. Neumanna, F. Pattena, E. Seibelc, and A. Nelson, "Automated cell analysis in 2D and 3D: A comparative study," *Pattern Recognition*, Vol. 42, 141–146, 2009.
6. Nandakumar, V., L. Kelbauskas, R. Johnson, and D. Meldrum, "Quantitative characterization of preneoplastic progression using single-cell computed tomography and three-dimensional karyometry," *Cytometry A*, Vol. 79, No. 1, 25–34, 2011.
7. Hajihashemi, M. R. and M. El-Shenawee, "Inverse scattering of three-dimensional PEC objects using the level-set method," *Progress In Electromagnetics Research*, Vol. 116, 23–47, 2011.
8. Hajihashemi, M. R. and M. El-Shenawee, "The level set shape reconstruction algorithm applied to 2D PEC targets hidden behind a wall," *Progress In Electromagnetics Research B*, Vol. 25, 131–154, 2010.
9. Hajihashemi, M. R. and M. El-Shenawee, "*TE* versus *TM* for the shape reconstruction of 2-D PEC targets using the level-set algorithm," *IEEE Trans. Geosci. & Rem. Sens.*, Vol. 48, No. 3, 1159–68, 2010.
10. Hajihashemi, M. R. and M. El-Shenawee, "Level set algorithm for shape reconstruction of non-overlapping three dimensional penetrable targets," *IEEE Trans. Geosci. & Rem. Sens.*, Vol. 50, No. 1, 75–86, Jan. 2012.
11. Salle, A. J., *Fundamental Principles of Bacteriology*, 2nd Edition, McGraw-Hill Book Co., 1943.
12. "Treatment of biological warfare agent casualties," ARMY FM 8-284, NAVY NAVMED P-5042, AIR FORCE AFMAN (I) 44-156, MARINE CORPS MCRP 4-11.1C, 2000.
13. El-Shenawee, M., O. Dorn, and M. Moscoso, "Adjoint-field

technique for shape reconstruction of 3-D penetrable object immersed in lossy medium", *IEEE Trans. Antennas and Propag.*, Vol. 57, No. 2, 520–534, Feb. 2009.

14. Querry, M., B. Curnuttea, and N. Williams, "Refractive index of water in the infrared," *J. of the Optical Society of America*, Vol. 59, No. 10, 1969.
15. Liebe, H., G. Hufford, and T. Manabe, "A model for the complex permittivity of water at frequencies below 1 THz," *Int. Journal of Infrared and Millimeter Waves*, Vol. 12, No. 7, 659–675, 1991.
16. Palmer, K. and D. Williams, "Optical properties of water in the near infrared," *J. of the Optical Society of America*, Vol. 64, No. 8, 1974.
17. Kotnik, T., and D. Miklavčič, "Second-order model of membrane electric field induced by alternating external electric fields," *IEEE Trans. on Biomed. Eng.*, Vol. 47, No. 8, 1074–1081, 2000.
18. Dubois, P., C. Dedeban, and J. Zolésio, "3D inverse scattering by level set with zero capacity connecting set. Wave guide optimization by 'zone'," *Proceedings of the First European Conference on Antennas and Propagation*, 1–6, 2006.
19. Hajihashemi, M. R. and M. El-Shenawee, "High performance computing of the level-set reconstruction algorithm," *Journal of Parallel and Distributed Computing*, Vol. 70, 671–679, Jun. 2010.
20. Hassan, A. M., M. R. Hajihashemi, M. El-Shenawee, A. Al-Zoubi, and A. Kishk, "Drift de-noising of experimental TE measurements for imaging 2D PEC cylinder using the level set algorithm," *IEEE Antennas and Wireless Propagation Letters*, Vol. 8, 1218–1222, 2009.
21. Woten, D. A., M. R. Hajihashemi, A. M. Hassan, and M. El-Shenawee, "Experimental microwave validation of level-set reconstruction algorithm," *IEEE Trans. Antennas and Propag.*, Vol. 58, No. 1, 230–233, Jan. 2010.
22. Karpowicz, N., J. Chen, T. Tongue, and X.-C. Zhang, "Coherent millimeter wave to mid-infrared measurements with continuous bandwidth reaching 40 THz," *Electronics Letters*, Vol. 44, 544–545, 2008.
23. Liu, J., J. Dai, X. Lu, I. Ho, and X.-C. Zhang, "Broadband terahertz wave generation, detection and coherent control using terahertz gas photonics," *International Journal of High Speed Electronics and Systems*, Vol. 20, No. 1, 3–12, 2011.
24. Bevilacqua, F., A. Berger, A. Cerussi, D. Jakubowski, and B. Tromberg, "Broadband absorption spectroscopy in turbid

media by combined frequency-domain and steady-state methods," *Applied Optics*, Vol. 39, No. 34, 6498–6507, Dec. 2000.